Soft Matter

Competing Forces on a Liquid Bridge between Parallel and Orthogonal Dissimilar Fibers

Journal:	*Soft Matter*
Manuscript ID	SM-ART-03-2019-000489.R1
Article Type:	Paper
Date Submitted by the Author:	14-Jul-2019
Complete List of Authors:	Aziz, Hossain; Virginia Commonwealth University, Mechanical and Nuclear Engineering Tafreshi, Hooman Vahedi; Virginia Commonwealth University, Mechanical and Nuclear Engineering

ARTICLE

Competing Forces on a Liquid Bridge between Parallel and Orthogonal Dissimilar Fibers

Received 00th January 20xx,
Accepted 00th January 20xx

DOI: 10.1039/x0xx00000x

H. Aziz[a] and H. V. Tafreshi[*a]

This paper presents a detailed investigation on the mechanical forces acting on a liquid bridge between dissimilar fibers in parallel and orthogonal configurations. These forces were measured experimentally, using a sensitive scale, and were also predicted computationally, via numerical simulation. Special attention was paid to the fiber-fiber spacing at which the liquid bridge detached from the fibers, and to how a transition from an equilibrium liquid bridge to a spontaneously (time-dependent) detaching bridge took place. It was found that, while varying the spacing between the fibers affects a liquid bridge differently for fibers with different relative angles with respect to one another, the spacing at which the bridge detaches from the fibers is independent of the fibers relative angle. This paper also formulates the contribution of the geometrical and wetting properties of the fibers competing for the droplet that results from a liquid bridge detachment, and presents a mathematical expression to predict the fate of that droplet.

1 Introduction

Liquid bridge between two solid surfaces has been the focus of many previous studies for its ubiquitous presence in a variety of applications. The capillary force generated by a capillary bridge contributes to the adhesion force that frogs, insects, or geckoes create to climb a vertical surface.[1,2] For instance, a particular type of beetle can generate an adhesion force of more than 60 times its body weight thanks to an array of liquid bridges that forms between its feet and the surface on which it walks.[3] In industry, liquid bridge plays a crucial role in underground oil recovery[4,5] and granular systems,[6-8] wetting and liquid transport in coalescence filters and textiles,[9-17] design of magnetic hard-disks,[18] papermaking,[19] fiber-based microfluidics[20,21] and fuel cells[22,23] among many others.

Scientific research on liquid bridge started in 1805 by Young who investigated a liquid bridge formed between two flat plates to study the liquid surface tension.[24] Later, Gauss derived the Young-Laplace equation which predicts the equilibrium shape of an interface separating two immiscible fluids.[25] Since then, many others studied liquid bridge between smooth flat plates for its industrial relevance, and also for the simplicity of its axisymmetric profile. These include many pioneering investigations where the effects of surface roughness or contact angle hysteresis on the shape and stability of a capillary bridge were studied.[26-30] Significant attention has also been paid to the fluid mechanics of a liquid bridge between two spherical objects, or between a sphere and a flat plate. The main objective of these studies was to measure the forces between the involved surfaces in terms of the distance between them or as a function of their surface properties in the absence[31-33] or presence of gravity.[34,35]

Given the decades of research on different liquid bridges, very little attention has been paid to the case of a liquid bridge between two fibers. In contrast to most previous studies, a liquid bridge between two fibers does not have an axisymmetric profile. This makes it harder to develop a mathematical description for the 3-D shape of the bridge. The shape of a liquid bridge between two parallel cylinders with a small spacing and in the absence of gravity was first studied by Princen.[36] Later, Protiere et al.[37] modified Princen's equations to study how a liquid body transitions from a droplet shape to a long liquid bridge between two parallel fibers when varying the fiber–fiber spacing, fiber diameter, fiber's Young–Laplace contact angle (YLCA), or the liquid volume. Princen's equation was also used by Schellbach et al.[38] to propose a method to measure the contact angle of natural fibers. Virozub et al.,[39] Wu et al.,[40] and Bedarkar et al.[41] simulated the 3-D shape of a liquid bridge between two fibers and reported the capillary forces acting on the fibers as a function of fiber–fiber spacing or the relative angle between the fibers.[39] Duprat and Protiere,[42] Duprat et al.,[43] and Soleimani et al.[44] also studied the problem of a capillary bridge between two fibers but with the main focus on fiber deformation in response to capillary forces.

The study presented in this paper contributes to the above body of literature by presenting a one-on-one experiment–simulation comparison for a capillary bridge formed between

[a] Department of Mechanical and Nuclear Engineering, Virginia Commonwealth University, Richmond, Virginia 23284-3015. E-mail: htafreshi@vcu.edu
http://www.people.vcu.edu/~htafreshi/

Electronic Supplementary Information (ESI) available: See DOI: 10.1039/x0xx00000x

two fibers in parallel and orthogonal configurations in the presence of gravity. Our work compares measured and simulated capillary forces exerted on the fibers by the liquid bridge throughout the stretching process and especially at the moment of bridge detachment from one of the fibers. The detachment force, in particular, is compared to the force required to detach a pendent droplet (with the same volume as the liquid bridge) from the fibers. This work also presents, for the first time, the effects of fiber radius or fiber YLCA dissimilarities on the liquid bridge shape and the capillary forces exerted on the fibers at the moment of bridge detachment (collapse). Special attention is paid to discuss how the two fibers compete for the droplet during bridge detachment, and how their radius or YLCA dissimilarity plays a role in determining the fate of the resulting droplet.

The remainder of this article is structured as follows. The experimental setup and the computational technique used in the present study are described in Section 2. The general physics of a liquid bridge between two fibers is qualitatively discussed in Section 3. Our results are discussed in Section 4. This section includes the effects of fiber spacing on the capillary forces, detachment force, and the corresponding shape of the liquid bridge for two fibers (similar and different) in parallel and orthogonal configurations and liquid transfer between the two fibers after detachment. The conclusions drawn from our study are discussed in section 5.

2 Methods of Investigation

2.1 Experimental Setup

Our experimental set-up is shown in Fig. 1. Flurocarbon smooth casting fishing line with radii of 105.5 µm and 190.5 µm were used in our study. The YLCA for the fishing lines were obtained using an image-based method reported in our previous work.[45-47] In this image-based method, a droplet of known volume was deposited on the fiber and imaged. The same fiber-droplet system was simulated with Surface Evolver code for different YLCA values. The profiles of the droplet obtained from experiment and simulations were compared with one another to estimate the YLCA of the fiber. The same process was repeated for different droplet volumes. The experiment was conducted with the two fibers positioned horizontally above one another. The lower fiber was mounted on a 3-D printed holder placed on a Mettler Toledo AG104 balance having an accuracy of 0.1 mg.

The upper fiber was attached to another holder mounted on a Mitutoyo electronic height gauge. A New Era NE-300 syringe pump with an infusion rate ranging from 0.73 to 1200 µL/h was used to produce droplets with desired volumes. The liquid used for the experiment was a water-glycerol mixture (15% by weight) having a surface tension of 0.071 N/m (measured via the pendent droplet method using a DSA25E drop shape analyser), viscosity 1.53 mPa.s (measured using a Discovery HR—three hybrid rheometer), and a density of 1039 kg/m3 at 20° C.

The scale was zeroed at the start of the experiment. A droplet was placed on the upper fiber and a stable liquid bridge was formed by lowering the upper fiber until the droplet touched the lower fiber. The upper fiber was then moved upward slowly to stretch the liquid bridge until a spontaneous detachment process (where no additional stretching was needed to deform the liquid bridge) started. The force applied by the liquid bridge to the lower fiber was read on the scale and the force applied to the upper fiber was obtained by adding the weight of the liquid to that. The force applied to the upper fiber at the onset of spontaneous detachment is referred to here as the detachment force F_d. The liquid bridge stretching process was recorded by a Phantom Miro LAB340 high-speed camera at 100 frames per second.

To ensure that inertial and viscous effects were negligible during the experiments, we calculated the Weber and Capillary numbers, defined respectively, as $We = \rho U^2 d_l \sigma^{-1}$and $Ca = \mu U \sigma^{-1}$ (ρ, σ, U, and μ are density, surface tension, upper fiber velocity, and viscosity, respectively and $d_l = \sqrt[3]{6V_l/\pi}$ is the volume-equivalent diameter of the liquid bridge). With a Weber number of $We \ll 1$ and a Capillary number of $Ca \ll 0.1$, it was concluded that our experimental results were not affected by inertial or viscous effects.[48]

2.2 Modelling Liquid Bridge between Two Fibers

Stretching of the liquid bridge between fibers in our experiment can be considered a quasi-static process (up until the spontaneous detachment) since both the Capillary and Weber numbers are quite small in our study ($Ca \ll 0.1$ and $We \ll 1$). This allows us to simulate the liquid bridge stretching using a time-independent formulation such as the one implemented in SE code.[49] SE computes the equilibrium shape of a liquid body by minimizing the total potential energy of the system given as

$$E = \sigma \iint_{A_{la}} dA - \sigma cos\theta_{YL} \iint_{A_{sl}} dA + g \iiint_{V_l} z\rho dV \qquad (1)$$

Here, A_{la} is the area of the liquid-air interface (LAI), A_{sl} is the area of the solid-liquid interface (SLI), V_l is the volume of the liquid bridge, and g is the gravitational acceleration. It can be seen from Eq. 1 that, the total potential energy is the sum of the surface and gravitational energies (gravity needs to be included in the calculations for the range of droplet volumes considered here, 0.5 µL to 7.5 µL). The simulations start with a rectangular cuboid-shaped liquid body placed on two fibers. SE computes the energy of the LAI by computing the area of the LAI. It also calculates the area of the SLI A_{sl} to obtain the contribution of each fiber in the total energy of the system. The SLIs are constrained to remain on the cylindrical surface of the fibers. With SE, one can derive a path integral to account for the fiber-liquid interfacial area A_{sl} for each fiber and to compute fiber's contribution to the total energy of the system. For the case of two parallel fibers, the path integral for the

contribution to the total potential energy due to A_{sl} can be written as,

$$E_{sl} = \sigma cos\theta_{YL} \oint_{\partial A_{sl}} \left[\frac{yz}{\sqrt{x^2+z^2}}\hat{i} + \frac{yx}{\sqrt{x^2+z^2}}\hat{k}\right].d\hat{l} - \frac{\rho g}{2}\oint_{\partial A_{sl}} yz^2 dx \quad (2)$$

For the case of orthogonal fibers, Eq. 2 was used to compute E_{sl} for the lower fiber. The path integral for E_{sl} for the upper fiber can be written as,

$$E_{sl} = \sigma cos\theta_{YL} \oint_{\partial A_{sl}} \left[\frac{xz}{\sqrt{y^2+z^2}}\hat{j} + \frac{yx}{\sqrt{y^2+z^2}}\hat{k}\right].d\hat{l} + \frac{\rho g}{2}\oint_{\partial A_{sl}} xz^2 dy \quad (3)$$

SE needs to satisfy a constant-volume constraint (input) for the liquid bridge while minimizing the energy of the system. The volume under the LAI is computed by SE through computing the volumes of the vertical prisms formed between each facet of the LAI and the $z = 0$ plane. In order to compute the volume of the liquid bridgeV_l, SE needs to subtract the part of the volume of these vertical prisms from the total volume under the LAI. Since, the SLI was not represented by facets in the simulations, a path integral was then derived to find the volume under the LAI occupied by each fiber. For the case of parallel fibers, we obtain,

$$V_s = \oint_{\partial A_{sl}} zydx \quad (4)$$

For the case of orthogonal fibers, we used Eq. 4 for the lower fiber, and use Eq. 5 for the upper fiber.

$$V_s = \oint_{\partial A_{sl}} zxdy \quad (5)$$

Equations 2–5, allow SE to obtain an equilibrium shape for a liquid bridge with a volume of V_l between the two fibers (see Figure 2). In this figure, we considered a water-glycerol mixture (15% by weight) droplet with a volume of $V_l = 3.5$ µL on two fibers with a fiber–fiber spacing of $s = 2100$ µm, a fiber diameter of $r_f = 190.5$ µm, and an YLCA of $\theta_{YL} = 70^o$.

3 Physics of Liquid Bridge Between Fibers

Capillary bridge between two cylinders (filaments/fibers) in parallel configuration was first investigated by Princen[36] and later, by Wu et al.[40] and Protiere et al.[37] in the absence of gravity. The two main morphologies observed in these investigations were the barrel-shaped droplet (where droplet completely engulfs the two fibers) and the droplet-bridge (where the droplet partially wraps around the fibers). Figure 3 shows experimental and computational images of a liquid bridge with a volume of 3.5 µL between two fibers with a radius of 190.5 µm and a YLCA of $\theta_{YL} = 70^o$in parallel (Figs. 3a and 3b) and orthogonal (Figs. 3c and 3d) configurations (see also the videos in supplementary information). It can be seen for the case of parallel fibers that an asymmetric (about the y-z and x-y planes) droplet-bridge is formed at a small fiber spacing of $s = 600$ µm. In an earlier study by Farmer and Bird,[50] asymmetric droplet-bridge between two spherical particles were reported but in the absence of gravity. This indicates that gravity cannot be the main factor responsible for the observed asymmetry about the y-z plane (the asymmetry about the x-y plane is due to gravity). The asymmetric shape in fact corresponds to the lowest energy state for the fiber–droplet system at the given spacing. As the fiber spacing was increased, droplet-bridge penetrated more into the space between the fibers, although the asymmetry with respect to the y-z and x-y planes sustained till $s < 1500$ µm. Further increase in spacing from $s = 1500$ µm to $s = 2400$ µm resulted in the droplet-bridge becoming symmetric about the y-z plane but still remaining asymmetric with respect to the x-y plane. Note in this range of spacing that, the bridge becomes narrower on the top, which is in qualitative agreement with the work of Sun et al.[51] on liquid bridge between two parallel fibers.

Figures 3c and 3d show the evolution of the same droplet but when the fibers are orthogonal to one another. The shape of the liquid bridge in this case was neither a barrel-shaped droplet nor a droplet-bridge for $s \leq 750$ µm, and so we refer to it as the semi-barrel droplet in this paper. The semi-barrel droplet was not imaged (although observed) during the experiment due to difficulty in capturing images from a longitudinal view at small fiber spacing. Our numerical simulation results revealed a transition from the semi-barrel droplet to the droplet-bridge at a spacing of about 720 µm $< s < 780$ µm. This transition was also noted in the evolution of the energy of the system as a function of fiber–fiber spacing (only the case of orthogonal fibers) in Figure 3e. Overall, depending on the geometrical and wetting properties of the given droplet–fibers system, one of the barrel-shaped droplet, semi-barrel droplet, or droplet-bridge configurations can be expected to prevail.

For the experiment reported in Figure 3 (parallel and orthogonal fiber configurations), the liquid bridge becomes unstable for $s > 2400$ µm. This starts by droplet changing its shape spontaneously with no further increase in the fiber–fiber spacing, leading to detachment from the upper fiber. Images in the last column on the right side of Figures 3a-3d show the final equilibrium state of the liquid bridge between the fibers. Any increase in the fiber–fiber spacing results in liquid bridge detachment from the upper fiber (gravity helps the liquid to remain on the lower fiber).

Note that the comparison between experimental and computational liquid bridge perspective shapes in Figure 3a–3d is only qualitative. A more accurate (i.e., a more quantitative) comparison between such non-axisymmetric shapes requires imaging their 2-D cross-sectional contours in some (e.g., vertical) planes, which is not easy in our experimental setup. The final fiber–fiber spacing s_d and bridge width (on the upper fiber) w_d^u are measured and shown in Figure 3f for both parallel and orthogonal fiber configurations. Figure 4 shows the dynamic detachment process for the liquid bridge shown in Fig. 3. It can be seen that the dynamic detachment process accelerates as the liquid bridge proceeds towards the detachment.

4 Force Balance Analysis

Figure 5a shows a free body diagram for a liquid bridge between two parallel fibers. The upward force is the total reaction force N_1 from the upper fiber. The downward forces are the weight of the liquid bridge $\rho V_l g$ and the reaction force N_2 from the lower fiber. Here, N_1 and N_2represent the net reaction force. Due to the static equilibrium assumption for the liquid bridge, one can write,[34,35]

$$N_1 = N_2 + \rho V_l g = F \quad (6)$$

To avoid confusion, the forces acting on the upper and the lower fibers are denoted here as $F^u = F$ and $F^l = F - \rho V_l g$, respectively. The force acting on the liquid bridge can also be calculated at any fiber–fiber spacing by taking the derivative of the total potential energy of the droplet $E(s)$ i.e.

$$F(s) = \frac{dE}{ds} \quad (7)$$

Note that the force obtained from Eq. 7 is the force between the liquid bridge and the upper fiber since the gravity is downward. The vertical force exerted by the liquid bridge on the fibers is the resultant of the forces from three different sources. One is the vertical component of the surface tension force acting along the contact line, the other is the force due to Laplace pressure, and the last one is the buoyancy force (fiber's partial submersion in liquid bridge).[35] Note that as will be shown later in the next section, the contribution of buoyancy force in the interfacial force between a droplet and a fiber is quite negligible near the onset of dynamic detachment process. The total force acting on each fiber can be described as,

$$F^i = \sigma \int_{L^i} cos\alpha^i\,(l)dl - A_p^i \Delta P^i \pm \rho V_b^i g \quad (8)$$

where *i* = *l* or *u*, and α is the angle between the direction of the capillary force at each point on the contact line and the vertical direction (see Fig. 5b), A_p is the projected wetted area (see Fig. 5c), L is the length of the contact line (see Fig. 5d), ΔP is the droplet pressure near the fiber, and V_b is the volume of the submerged fiber (see Fig. 5c). The upper and lower planes shown in Fig. 5b were considered for calculating pressures ΔP^u and ΔP^l on the upper and lower fibers, respectively.

5 Results and Discussion

5.1 Liquid Bridge between Similar Fibers

We start this section by studying the effects of fiber–fiber spacing on the net force between the bridge and fibers for a system with a fiber diameter of $r_f = 190.5\ \mu\text{m}$, a YLCA of $\theta_{YL} = 70^o$, and a droplet volume of $V_l = 3.5\ \mu\text{m}$. Recall from the previous section that the liquid bridge between two fibers may have an asymmetric profile about the vertical planes passing through the fiber's axis when the spacing is small (leading to droplet morphological transitions).

Moreover, the liquid bridge between two closely-spaced parallel fibers has a tendency to slowly (but continuously) spread along the fibers in the form of a narrow liquid sheet. This prolongs the time to reach equilibrium and adds errors to the experiments.[20,52] For these reasons, we focused our experiments on the range of fiber–fiber spacing at which the droplet-bridge remains symmetric about the vertical planes passing through the fibers ($1500\ \mu\text{m} \le s \le 2400\ \mu\text{m}$ here). Figures 6a and 6b show the forces on the upper fiber for the parallel and orthogonal fiber configurations, respectively. It can be seen that the interfacial force between a bridge and the upper or lower fiber increases with increasing the spacing between the fibers. Good general agreement can be seen between the experimental and computational forces for all cases considered (upper and lower fibers in parallel and orthogonal configurations). To ensure the accuracy of our force analysis, we considered both the energy approach of Eq. 7 and the force balance method of Eq. 8, and both methods produced identical predictions, as can be seen in Figures 6a–6c). Note in these figures that the detachment force is the same for parallel and orthogonal fiber arrangements (see Fig. S1 in the supplementary information for detailed data analysis). Our results also revealed that the contribution of the buoyancy force in the detachment force is generally less than 1% (see Fig. S1e in the enclosed Supplementary Information). For this reason, buoyancy is not considered in our detachment force calculations in this paper.

We also considered a bridge between two more hydrophilic fibers ($\theta_{YL} = 30^o$) to confirm the above-mentioned behavior. It can interestingly be seen in Figure 7a that F^u becomes independent of the angle between the fibers δ right before spontaneous detachment process starts (i.e., at $s/r_f = 13.12$). However, F^u changed significantly with changing δ at small fiber spacing values. The value of F^u increases more than three times as the fiber orientation changes from the orthogonal position to the parallel position at $s/r_f = 5.77$ (see Figure 7a). This can be attributed to the fact that the shape of the liquid bridge (especially near the upper fiber) changes with changing δ at small fiber spacing (see Figure 7b). It can clearly be seen in Figure 7b that the width of the liquid bridge w^u near the upper fiber changes significantly with changing δ for $s/r_f = 5.77$. This is in agreement with the work of Sauret et al.[53] However, Fig. 7b also shows that the width of the liquid bridge w_d^u near the upper fiber for $s/r_f = 13.12$ (pre-detachment stage) is almost independent of δ.

The interfacial force between the upper fiber and the liquid bridge is mainly comprised of surface tension force acting along the contact line $\left(F_{cl}^u = \sigma \int_{L^u} cos\,\alpha^u(l)dl\right)$ and the force due to Laplace pressure $\left(F_p^u = A_p^u \Delta P^u\right)$. We found from our simulations that the surface tension force tends to hold the droplet in contact with the fibers while the Laplace pressure force tends to detach the droplet from the fibers for all the cases we investigated. The force between the upper fiber and the liquid bridge is therefore the resultant of these two forces. Figure 8a shows the variation of capillary force F_{cl}^u with θ_{YL} for a liquid bridge with a volume of $V_l = 3.5\ \mu\text{L}$ between parallel fibers with a radius of $r_f = 190.5\ \mu\text{m}$. It can be seen that F_{cl}^u

decreases with increasing θ_{YL}. However, the changes in F_p^u is negligible compared to those in F_{cl}^u (i.e., F_{cl}^u becomes a more dominant force when decreasing θ_{YL}, as can be seen in Fig. 8b). As a result, the interfacial force between the upper fiber and the liquid bridge increases with decreasing θ_{YL}. Figure 8a also shows that F_p^u monotonically decreases with fiber-fiber spacing, in contrast to F_{cl}^u which only slightly increases initially but then decreases (also slightly) with increasing s. Overall, the ratio of F_{cl}^u to F_p^u increases monotonically with increasing fiber-fiber spacing (see Figure 8b). It should be noted in Figure 8b that this ratio becomes independent of θ_{YL} near the detachment moment. Figure 8c shows the effects of fiber radius r_f on F_{cl}^u and F_p^u for $\theta_{YL} = 30^o$ and a bridge volume of $V_l = 3.5\ \mu L$. It can be seen that both F_{cl}^u and F_p^u increase with increasing r_f, and F_{cl}^u continues to be greater than F_p^u. For this case also, the ratio of F_{cl}^u to F_p^u monotonically increases with s (see Fig. 8d).

Referring to the force applied to the upper fiber at the moment of detachment as F_d^u, Figure 9a shows the detachment force versus droplet volume for parallel and orthogonal fibers with two different YLCAs of $\theta_{YL} = 30^o$, and $\theta_{YL} = 70^o$but a radius of $r_f = 190.5\ \mu m$. It can again be seen that the detachment force does not depend on the orientation of the fibers relative to each other (liquid bridge detached from the upper fiber in all cases reported in Figure 9a). The detachment force between the liquid bridge and the fibers depends on the length of the contact line, angle between the direction of surface tension force and the vertical direction, droplet pressure, and the projected wetted area of the fibers at $s = s_d$ (see Fig. S2 and related discussion in Supplementary Information for a detailed data analysis).

It can be seen that the detachment force decreases with increasing the YLCA. Detachment force was also measured experimentally for fibers having a YLCA of $\theta_{YL} = 55^o$ (with $r_f = 105.5\ \mu m$), and the results are added to Figure 9b. Excellent agreement can again be seen between the experimental and computational results.

5.2 Liquid Bridge between Dissimilar Fibers

In this section, we present our results for a liquid bridge between fibers having different radii and/or YLCAs. To do so, we considered an upper fiber with a radius of $r_f^u = 105.5\ \mu m$ and a YLCA of $\theta_{YL}^u = 55^o$, but a lower fiber with a radius of $r_f^l = 190.5\ \mu m$ and a YLCA of $\theta_{YL}^l = 70^o$.

Figure 10a shows examples of a liquid bridge with a volume of $V_l/r_f^{u3} = 2129$ between the above-mentioned fibers from experiment and simulation at the moment of detachment. Figure 10b shows the detachment force for liquid bridges of different volumes in parallel and orthogonal fiber configurations. The figure also includes the detachment force obtained using a lower fiber identical to the upper fiber for comparison. It can be seen that detachment force does not depend on the relative angle between the fibers or on the radius and YLCA of the lower fiber, as long as the detachment is from the upper fiber. Additional computational data are given in the supplementary information (see Fig. S3) in support of the results shown in Figure 10b. However note that, if the lower fiber is much bigger in diameter (or is much more hydrophilic) than the upper fiber, then the detachment may happen at a smaller spacing. This was observed in a series of SE simulations conducted for the same upper fiber but a lower fiber with a radius of $r_f^l = 500\ \mu m$ and a YLCA of $\theta_{YL}^l = 30^o$ for a liquid volume in the range of $425.8 \le V_l/r_f^{u3} \le 2129$.

The detachment force can be regarded as a factor that determines whether or not a droplet originally on the upper fiber will move to the lower fiber after detachment. While a droplet would obviously move to the lower fiber after detachment when the fibers are identical (due to gravity), the same cannot be said for when the fibers have different physical and/or wetting properties. The latter depends on the interfacial forces between the droplet and the fibers. In fact, if the detachment force of the upper fiber is greater than the sum of the detachment force of the lower fiber and the weight of the droplet (i.e.,$F_d^u > F_d^l + \rho V_l g$), then the droplet most probably remains on the upper fiber after the detachment.

Consider a liquid bridge with a volume of $V_l = 2.5\ \mu L$ between an upper fiber with $r_f^u = 105.5\ \mu m$ and $\theta_{YL}^u = 55^o$, and a lower fiber with $r_f^l = 190.5\ \mu m$ and $\theta_{YL}^u = 70^o$ (Figure 11a). In this case, detachment forces for the upper and lower fibers can be found to be $F_d^u = 84.72\ \mu N$ and $F_d^l = 97.6\ \mu N$, respectively. The droplet therefore remains with the lower fiber after detachment. Swapping the fibers, will not change this outcome as $F_d^u = 97.6\ \mu N$ will still be smaller than $F_d^l + \rho V_l g = 84.72 + 25.48\ \mu N = 110.2\ \mu N$, as can be seen in Figure 11b). Figure 11c however shows the case where the same droplet is placed between an upper fiber with $r_f^u = 264.1\ \mu m$ and $\theta_{YL}^u = 30^o$, and a lower fiber with $r_f^l = 105.5\ \mu m$ and $\theta_{YL}^l = 55^o$. The detachment force for the upper fiber is now $F_d^u = 142.2\ \mu N$ which is greater than $F_d^l = 84.72\ \mu N$ plus the weight of the droplet (i.e.,$84.72 + 25.48\ \mu N = 110.2\ \mu N$), and so the droplet remains on the upper fiber. It is therefore evident that the outcome of a liquid bridge detachment experiment can be predicted using quantitative information about the detachment force of the individual fibers.

In a recent study, Farhan and Tafreshi[47] proposed a correlation to predict the force required to detach a pendent droplet from a fiber (see also the work of Ojaghlou et al.[54]). Since the detachment force investigated in the present study depends mainly on the properties of the fiber from which the droplet detaches, we compared our results with the detachment force values from the correlation of Farhan and Tafreshi[47] in Figure 11d. It can be seen that the detachment forces obtained in the present study are about 15–20% lower than those obtained from the above correlation. This difference can be attributed to the differences between the shape of a detaching pendent droplet and that of a detaching liquid bridge. Nevertheless, given the close agreement between the two, the correlation of

Farhan and Tafreshi[47] is used in this study to determine if a droplet resulting from liquid bridge detachment remains on the upper fiber or if it moves to the lower fiber. We expect the droplet to remain on the upper fiber if the following criterion is satisfied.

$$\left(\frac{r_{ref}}{r_f^u}\right)^2 \frac{\sigma}{\sigma_{ref}}(1+\cos\theta_{YL}^u)\varphi\left(\frac{V_l}{r_f^{u3}}\right)^{\xi}\left(1-\frac{R_r^{2+3\xi}}{R_\theta}\right) > g \qquad (9)$$

Here $\varphi = 3894$, $\xi = -0.84$, $\sigma_{ref} = 0.0649$ N/m, $r_{ref} = 190.5 \times 10^{-6}$ m, $R_r = r_f^u/r_f^l$, and $R_\theta = (1+\cos\theta_{YL}^u)/(1+\cos\theta_{YL}^l)$.

Equation 9 can be of great value to applications like fog harvesting[55-60], coalescence filtration[11-17], fibrous membrane[61-67], and even future stretchable electronics[68] or additive manufacturing processes[69] among many others,[4,5,19-23,70] where liquid droplets have to travel through a network of vibrating and/or deforming fibers, and where the rate of droplet transport depends on how the fibers compete for the droplet (in the presence of gravitational and/or a hydro/aerodynamic fields).

Although Eq. 9 is easy to use, it is difficult to get a physical understanding of the fate of the droplet resulting from liquid bridge detachment because of its complexity. A better physical understanding of this system can be obtained with the help of a phase diagram. However, the challenge in creating such a phase diagram is that the fate of this droplet will depend on the radius of the upper fiber, ratio between the radii of the upper and lower fibers, YLCAs of the upper and the lower fibers, and the volume of the liquid bridge. Therefore, such a phase diagram will have to have 5 dimensions, which makes it very hard to plot. To simplify the problem, we therefore present a phase diagram for the case of an upper fiber having a radius of $r_f^u = 105.5$ μm, an YLCA of $\theta_{YL}^u = 55^o$. We also assumed a liquid bridge with a volume of $V_l = 0.5$ μL (see Figure 12a). We chose $R_r = r_f^u/r_f^l$ as the x-axis and $R_\theta = (1+cos\,\theta_{YL}^u)/(1+cos\,\theta_{YL}^l)$ as the y-axis. The dark blue region corresponds to the R_r and R_θ values for which the droplet will move to the lower fiber, and the yellow region corresponds to the case where droplet moved to the upper fiber. It can be seen that as R_r increases the height of the dark blue zone decreases. This indicates that the minimum lower-fiber YLCA at which the droplet moves to the upper fiber decreases with decreasing the radius of the lower fiber. It can also be seen in Fig 12a that the droplet moves to the upper fiber irrespective of the YLCA of the lower fiber for $R_r > 1.8$. Figure 12b shows the phase diagram for same upper fiber but with a liquid bridge volume of $V_l = 2.5$ μL. Note that, the droplet moves to the upper fiber irrespective of the YLCA of the lower fiber for $R_r > 3$.

Conclusions

Experiments and numerical simulations were devised to study a liquid bridge formed between two parallel or orthogonal fibers with similar or dissimilar geometrical or wetting properties. It was quantitatively shown that the 3-D shape of the liquid bridge and its interactions with the fibers vary significantly with varying the spacing between the fibers. Focusing on the transition from a liquid bridge in equilibrium to one that is detaching from one of the fibers spontaneously, it was shown that the relative angle between the fibers does not affect the outcome of a liquid bridge detachment (i.e., the fiber–fiber spacing at which detachment occurs is independent of the angle between the fibers). It was also shown that the liquid bridge detaches from the fiber that provides a weaker capillary force (after factoring the weight of the liquid), and the force needed for detachment does not strongly depend on the size or the YLCA of the other fiber (as long as it provides a larger capillary force, of course). It was also shown that a mathematical criterion can be developed to predict which of the two fibers accommodating a liquid bridge will take the droplet that results from the bridge detachment.

Conflicts of interest

There are no conflicts to declare.

Acknowledgements

The authors acknowledge the financial support from the National Science Foundation CBET (1402655) program and VCU.

References

1 G. Hanna, and W.J.P. Barnes, *J. Exp. Biol.*, 1991, **155**, 103 – 125.
2 G. Huber, H. Mantz, R. Spolenak, K. Mecke, K. Jacobs, S.N. Gorb, E. Arzt, *PNAS*, 2005, **102**(45), 16293 – 16296.
3 T. Eisner, and D.J. Aneshansley, *PNAS*, 2000, **97**(12), 6568 – 6573.
4 M. Dejam, H. Hassanzadeh, Z. Chen, *Journal of Hydrology*, 2014, **519**, 3520-3530.
5 S. Hu, and C.A. Koh, *Langmuir*, 2017, **33**, 11299-11309
6 L. Bocquet, E. Charlaix, S. Ciliberto, J. Crassous, *Nature*, 1998, **396**(6713), 735 – 737.
7 Z. Fournier, D. Geromichalos, S. Herminghaus, M.M. Kohonen, F. Mugele, M. Scheel, M. Schulz, B. Schulz, C. Schier, R. Seemann, A. Skudelny, *J. Phys.: Condens. Matter*, 2005, **17**, S477 – S502.
8 M. Scheel, R. Seemann, M. Brinkmann, M. Di Michiel, A. Sheppard, B. Breidenbach, S. Herminghaus, *Nature Materials*, 2008, **7**, 189 – 193.
9 A. Patnaik, R.S. Rengasamy, V.K. Kothari, A. Ghosh, *Text. Prog.*, 2006, **38**, 1 – 105.
10 B.J. Mullins, I.E. Agranovski, R.D. Braddock, C.M. Ho, *J. Colloid Interface Sci.*, 2004, **269**, 449 – 458.
11 D. Kampa, S. Wurster, J. Buzengeiger, J. Meyer, G. Kasper, *Int. J. Multiphase Flow*, 2014, **58**, 313 – 324.
12 S.U. Patel, and G.G. Chase, *Sep. Purif. Technol.*, 2014, **126**, 62 – 68.

13 Y. Yu, H. Chen, Y. Liu, V.S.J. Craig, Z. Lai, *Adv Colloid Interface Sci.*, 2016, **235**, 46 – 55.
14 S. Wurster, D. Kampa, J. Meyer, T. Muller, B.J. Mullins, G. Kasper, *Chem. Eng. Sci.*, 2015, **132**, 72 – 80.
15 X. Wei, H. Zhou, F. Chen, H. Wang, Z. Ji, T. Lin, *Adv. Funct. Mater.*, 2019, **29**(1), 1806302.
16 C.J. Hotz, R. Mead-Hunter, T. Becker, A.J.C. King, S. Wurster, G. Kasper, B.J. Mullins, *J. Fluid Mech.*, 2015, **771**, 327 – 340.
17 R.P. Sahu, S. Sinha-Ray, A.L. Yarin, B. Pourdeyhimi, *Soft Matter*, 2013, **9**, 6053.
18 S.K. Chilamakuri, and B. Bhushan, *J. Appl. Phys.*, 1999, **86**(8), 4649.
19 T.G.M. van de Ven, *Ind. Eng. Chem. Res.*, 2008, **47**, 7250 – 7256.
20 K. Keis, K.G. Kornev, A.V. Neimark, Y.K. Kamath, *NATO Science series II: Mathematics, Physics and Chemistry, Kluwer publishing*, 2004, **169**, 175 – 182.
21 T. Gilet, D. Terwagne, N. Vandewalle, *Appl. Phys. Lett*., 2009, **95**, 014106.
22 E. Gauthier, T. Hellstern, I.G. Kevrekidis, J. Benziger, *ACS Appl. Mater. Interfaces*, 2012, **4**, 761 – 771.
23 V. Garau, M.J. Bluemle, E.S.D. Castro, Y.M. Tsou, J.A. Man Jr, T.A. Zawodzinski, *J. Power Sources*, 2006, **160**(2), 1156 – 1162.
24 T. Young, *Philos. Trans. R. Soc. London*, 1805, **95**, 65 – 87.
25 R. Finn, Capillary surface interfaces. *Not AMS*, 1999, **46**, 770 – 781.
26 E.J. De Souza, M. Brinkmann, C. Mohrdieck, A. Crosby, E. Arzt, *Langmuir*, 2008, **24**, 10161 – 10168.
27 E.J. De Souza, L. Gao, T.J. McCarthy, E. Arzt, A.J. Crosby, *Langmuir*, 2008, **24**(4), 1391 – 1396.
28 H. Chen, A. Amirfazli, T. Tang, *Langmuir*, 2013, **29**, 3310 – 3319.
29 H. Kusumaatmaja, and R. Lipowsky, *Langmuir*, 2010, **26**(24), 18734 – 18741.
30 B. Qian, and K.S. Breuer, *J. Fluid Mech.*, 2011, **666**, 554 – 572.
31 H-J. Butt., *Langmuir*, 2008, **24**(9), 4715 – 4721.
32 L. Vagharchakian, R. Restagno, L. Leger, *J. Phys. Chem. B*, 2009, **113**, 3769 – 3775.
33 C.D. Willet, M.J. Adamd, S.A. Johnson, J.P.K. Seville, *Langmuir*, 2000, **16**, 9396 – 9405.
34 D.N. Mazzone, G.I. Tardos, R. Pfeffer, *Journal of Colloid and Interface Science*, 1986, **113**(2), 544 – 556.
35 M.J. Adams, S.A. Johnson, P.K. Seville, C.D. Willet, *Langmuir*, 2002, **18**, 6180 – 6184.
36 H.M. Princen, *Journal of Colloid and Interface Science*, 1970, **34**(2), 171 – 184.
37 S. Protiere, C. Duprat, H.A. Stone, *Soft Matter*, 2013, **9**, 271.
38 S.L. Schellbach, S.N. Monteiro, J.W. Drelich, *Materials Letters*, 2016, **164**, 599 – 604.
39 A. Virozub, N. Haimovich, S. Brandon, *Langmuir*, 2009, **25**(22), 12837 – 12842.
40 X-F. Wu, A. Bedarkar, K.A. Vaynberg, *Journal of Colloid and Interface Scinece*, 2010, **341**, 326 – 332.
41 A. Bedarkar, X-F. Wu, A. Vaynberg, *Applied Surface Science*, 2010, **256**, 7260 – 7264.
42 C. Duprat, and S. Protiere, *EPL*, 2015, **111**, 56006.
43 C. Duprat, S. Protiere, A.Y. Beebe, H.A. Stone, *Nature*, 2012, **482**, 510 – 513.
44 M. Soleimani, R.J. Hill, T.G.M. van de Ven, *Langmuir*, 2015, **31**, 8328 – 8334.
45 M.M. Amrei, D.G. Venkateshan, N. D'Souza, J. Atulasimha, H.V. Tafreshi, *Langmuir*, 2016, **32**, 13333 – 13339.
46 H. Aziz, N.M. Farhan, H.V. Tafreshi, *Experiments in Fluids*, 2018, **59**, 122.
47 N.M. Farhan, and H.V. Tafreshi, *J. Appl. Phys.*, 2018, **124**, 075301.
48 P. Gopalkrishan, I. Manas-Zloczower, D.L. Feke, *Advanced Powder Technology*, 2008, **19**, 277 – 292.
49 K.A. Brakke, Surface Evolver manual version 2.50, 2012.
50 T.P. Farmer, and J.C. Bird, *Journal of Colloid and Interface Science*, 2015, **454**, 192 – 199.
51 X. Sun, H.J. Lee, S. Michielsen, E. Wilusz, *Applied Surface Science*, 2018, **441**, 791 – 797.
52 A. Ponomarenko, D. Quere, C. Clanet, *J. Fluid Mech.*, 2011, **666**, 146 – 154.
53 A. Sauret, F. Boulogne, B. Soh, E. Dressaire, H.A. Stone, *Eur. Phys. J. E*, 2015, **38**, 62.
54 N. Ojaghlou, H.V. Tafreshi, D. Bratko, A. Luzar, *Soft Matter*, 2018, **14**, 8924.
55 D. Seo, J. Lee, C. Lee, Y. Nam, *Scientific Reports,* 2016, **6**, 24276.
56 F. Weyer, A. Duchesne, N. Vandewalle, *Scientific Reports*, 2017, **7**, 13309.
57 F. Weyer, M. Lismont, L. Dreesen, N. Vandewalle, *Soft Matter*, 2015, **11**, 7086.
58 Z. Pan, F. Weyer, W.G. Pitt, N. Vandewalleb, T.T. Truscott, *Soft Matter*, 2018, **14**, 3724.
59 N.M. Farhan and H.V. Tafreshi, *Langmuir,* 2019, **35,** 8490
60 W. Shi, M.J. Anderson, J.B. Tulkoff, B.S. Kennedy, J.B. Boreyko, *ACS Appl. Mater. Interfaces*, 2018, **10**, 11979.
61 F. Guo, A. Servi, A. Liu, K.K. Gleason, G.C. Rutledge, *ACS Appl. Mater. Interfaces,* 2015, **7**, 8225 – 8232.
62 Y. Liao, C-H Loh, R. Wang, A.G. Fane, *ACS Appl. Mater. Interfaces,* 2014, **6**, 16035 – 16048.
63 M. Jamali, A. Moghadam, H.V. Tafreshi, B. Pourdeyhimi, *Applied Surface Science*, 2018, **456**, 626 - 636.
64 M. Jamali, H.V. Tafreshi, B. Pourdeyhimi, *Langmuir*, 2018, **34**, 12488.
65 H. Yu, M. Rump, S. Maheshwari, L. Bao, and X. Zhang, *Phys. Chem. Chem. Phys.*, 2018, **20**, 18252.
66 S. Narayan, D.B. Moravec, B.G. Hauser, A.J. Dallas, and C.S Dutcher, Energy Fuels 2018, **32**, 7326.
67 M. Jamali, H.V. Tafreshi, B. Pourdeyhimi, *J. Appl. Phys.*, 2019, **125**, 145304.
68 P. Grandgeorgea, A. Antkowiak, S. Neukirch, *Advances in Colloid and Interface Science*, 2018, **225**, 2.
69 K. Pich, J. Samuel, *Journal of Manufacturing Processes*, 2018, **32**, 816.
70 S. Mehrabian, F. Letendre, C.B. Cameron, *Marine Environmental Research*, 2018, **135**, 29.

Figure Captions

Figure 1: The experimental setup designed for study.

Figure 2: Liquid bridge 3-D shape obtained from SE simulations for a water-glycerol droplet with a volume of $V_l = 3.5$ μL between two fibers in parallel and orthogonal configurations. Fiber radius, YLCA and fiber-fiber spacing are $r_f = 190.5$ μm, $\theta_{YL} = 70^o$, and $s = 2100$ μm respectively.

Figure 3: Variation of liquid bridge 3-D shape with fiber-fiber spacing is obtained: (a) from experiment in parallel position; (b) from simulation in parallel position; (c) from experiment in orthogonal position; and (d) from simulation in orthogonal position. In all cases $r_f = 190.5$ μm, $\theta_{YL} = 70^o$, $V_l = 3.5$ μL, and the liquid is a water-glycerol mixture (15%). Droplet energy versus spacing is given in (e). Final droplet width on the upper fiber w_d^u and final fiber-fiber spacing s_d are also given in (f) versus droplet volume.

Figure 4: Spontaneous detachment process for parallel (a) and

orthogonal (b) fiber configurations for $r_f = 190.5$ μm, $\theta_{YL} = 70^o$, and $V_l = 3.5$ μL.

Figure 5: A free body diagram for a liquid bridge between two parallel fibers is shown in (a). The immersion angle α for the upper and lower fibers, the planes at which the pressure forces are calculated are shown in (b). Wetted area and three phase contact line are shown in (c) and (d) respectively, for the upper and lower fibers.

Figure 6: Interfacial force between the upper fiber and the liquid bridge versus fiber spacing for fibers in parallel (a) and orthogonal (b) configurations. Interfacial forces between the lower fiber and the liquid bridge versus fiber spacing are shown in (c). For all cases, $r_f = 190.5$ μm, $\theta_{YL} = 70^o$, and $V_l = 3.5$ μL with the water-glycerol (15%) mixture as the liquid. Each force data point is an average value obtained from six repetition. The error bars represent spread of data about the mean value.

Figure 7: (a) Interfacial force between the upper fiber and the liquid bridge versus fiber spacing for different fiber orientations. (b) Shapes of the liquid bridge for $\delta = 0^o, 45^o$ and 90^o at $S/r_f = 5.77$ and $S/r_f = 13.12$. Here, $r_f = 190.5$ μm, $\theta_{YL} = 30^o$, and $V_l = 3.5$ μL with water-glycerol (15%) mixture as the liquid.

Figure 8: (a) Variation of the vertical component of the surface tension force acting along the contact line of the upper fiber F_{cl}^u and the force on the upper fiber due to Laplace pressure F_p^u with fiber-fiber spacing s for $\theta_{YL} = 30^o, 50^o$ and 70^o and $r_f = 190.5$ μm. (b) Variation of the ratio between F_{cl}^u and F_p^u with s for $\theta_{YL} = 30^o, 50^o$ and 70^o and $r_f = 190.5$ μm. (c) Variation of F_{cl}^u and F_p^u with s for and $r_f = 190.5$ μm and 300 μm and $\theta_{YL} = 30^o$. (d) Variation of the ratio between F_{cl}^u and F_p^u with s for and $r_f = 190.5$ μm and 300 μm and $\theta_{YL} = 30^o$. For all the cases, $V_l = 3.5$ μL and fiber configuration is parallel.

Figure 9: Detachment force F_d^u (non-dimensionalized by $4\pi\sigma r_f$) versus liquid volume for different θ_{YL} (a) and different fiber radius r_f (b) with water-glycerol (15%) mixture as the liquid.

Figure 10: (a) Liquid bridge between parallel and orthogonal dissimilar fibers having different radius and wettability from experiment and simulation. (b) Detachment force F_d^u (non-dimensionalized by $4\pi\sigma r_f^u$) vs normalized liquid volume for the upper and lower fibers with different properties.

Figure 11: Droplet transfer between the upper and lower fibers for the case of $r_f^u = 105.5$ μm, $\theta_{YL}^u = 55^o$, $r_f^l = 190.5$ μm, and $\theta_{YL}^l = 70^o$ (a), $r_f^u = 190.5$ μm, $\theta_{YL}^u = 70^o$, $r_f^l = 105.5$ μm, and $\theta_{YL}^l = 55^o$ (b), $r_f^u = 264.1$ μm, $\theta_{YL}^u = 30^o$, $r_f^l = 105.5$ μm, and $\theta_{YL}^l = 55^o$ (c). Comparison between the detachment forces obtained in the present study and those of the correlation of Farhan and Tafreshi47 is given in (d).

Figure 12: Phase diagram showing the fate of the droplet resulting from the liquid bridge detachment for the case of liquid bridge volume (a) $V_l = 0.5$ μL and (b) $V_l = 2.5$ μL with $r_f^u = 105.5$ μm and $\theta_{YL}^u = 55^o$.

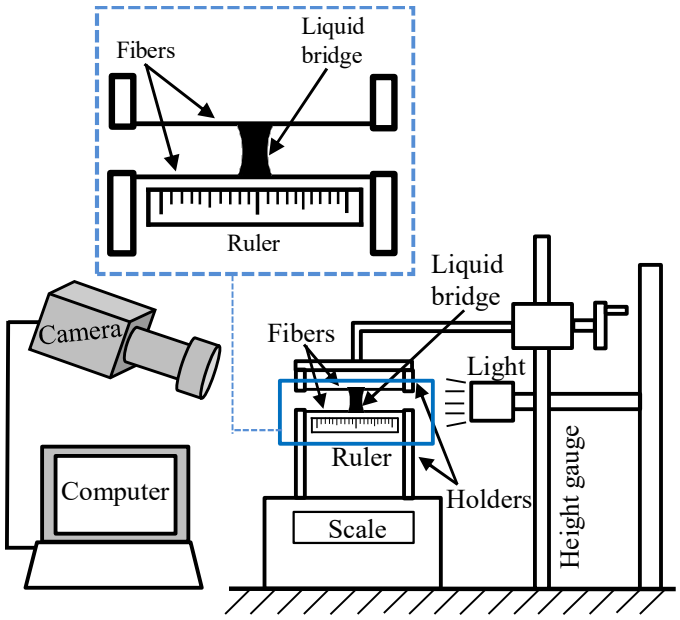
Fibers
Liquid bridge
Ruler
Liquid bridge
Camera
Fibers
Light
Ruler
Computer
Holders
Scale
Height gauge

Fig. 1

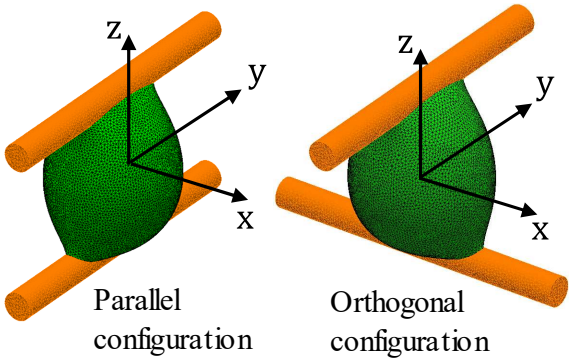
z
y
x
Parallel
configuration
z
y
x
Orthogonal
configuration

Fig. 2

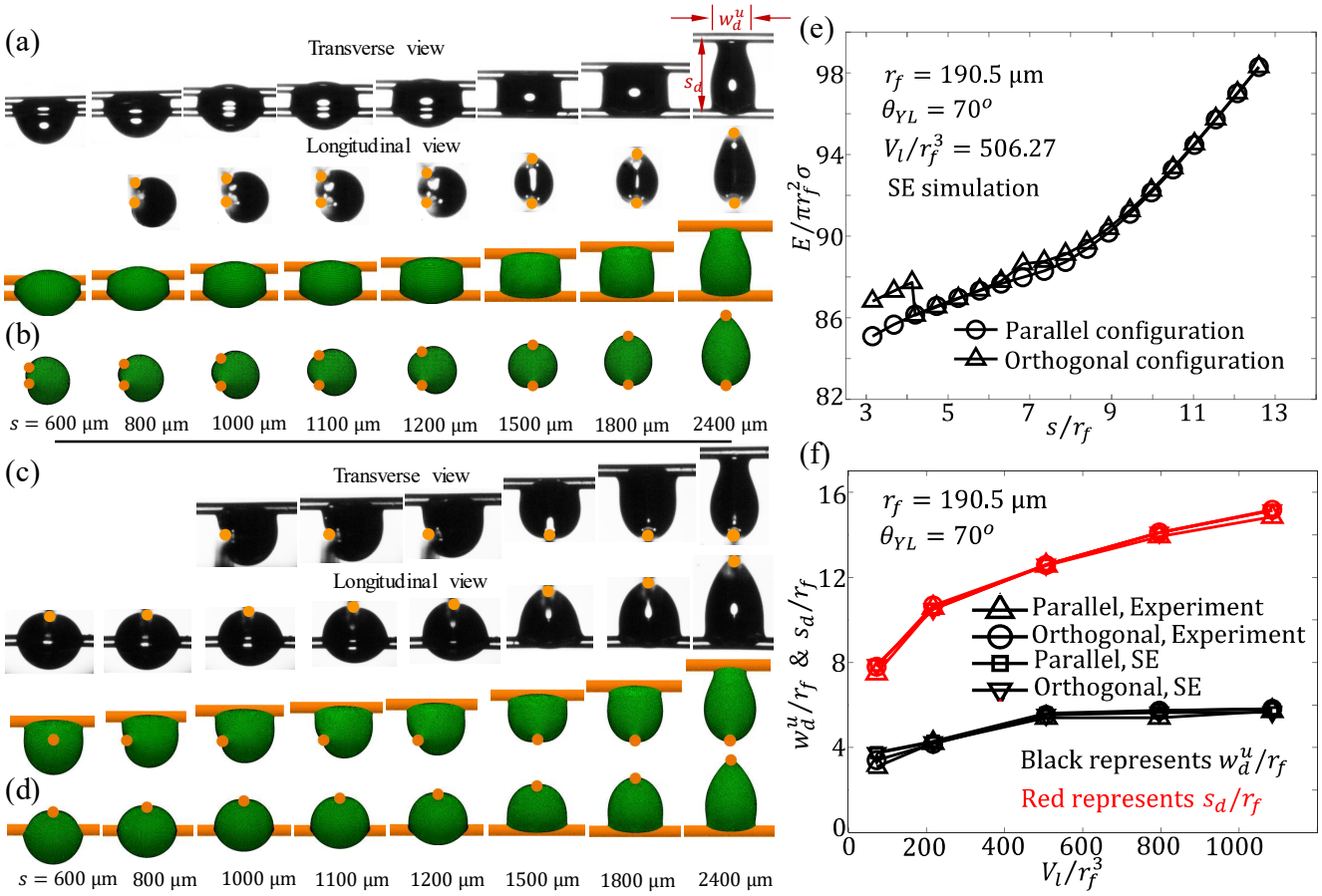
(a)
Transverse view
Longitudinal view
(b)
s = 600 μm 800 μm 1000 μm 1100 μm 1200 μm 1500 μm 1800 μm 2400 μm
(c)
Transverse view
Longitudinal view
(d)
s = 600 μm 800 μm 1000 μm 1100 μm 1200 μm 1500 μm 1800 μm 2400 μm
(e)
$r_f = 190.5$ μm
$\theta_{YL} = 70^o$
$V_l/r_f^3 = 506.27$
SE simulation
Parallel configuration
Orthogonal configuration
$E/\pi r_f^2\sigma$
s/r_f
(f)
$r_f = 190.5$ μm
$\theta_{YL} = 70^o$
Parallel, Experiment
Orthogonal, Experiment
Parallel, SE
Orthogonal, SE
Black represents w_d^u/r_f
Red represents s_d/r_f
w_d^u/r_f & s_d/r_f
V_l/r_f^3

Fig. 3

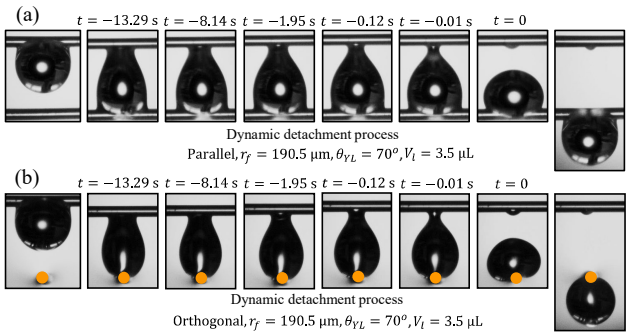
(a)
$t = -13.29$ s
$t = -8.14$ s
$t = -1.95$ s
$t = -0.12$ s
$t = -0.01$ s
$t = 0$
Dynamic detachment process
Parallel, $r_f = 190.5$ μm, $\theta_{YL} = 70^o$, $V_l = 3.5$ μL
(b)
$t = -13.29$ s
$t = -8.14$ s
$t = -1.95$ s
$t = -0.12$ s
$t = -0.01$ s
$t = 0$
Dynamic detachment process
Orthogonal, $r_f = 190.5$ μm, $\theta_{YL} = 70^o$, $V_l = 3.5$ μL

Fig. 4

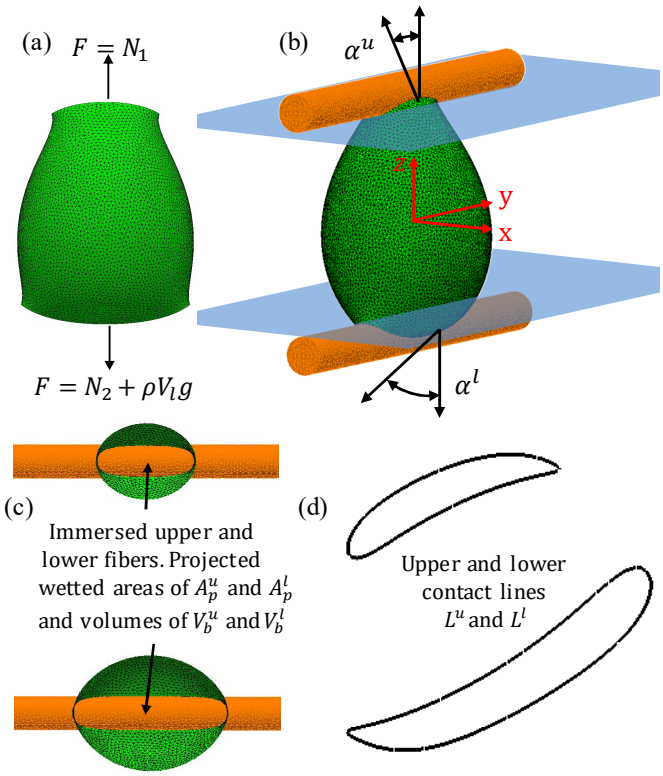
(a)
$F = N_1$
$F = N_2 + \rho V_l g$
(b)
α^u
α^l
z
y
x
(c)
Immersed upper and lower fibers. Projected wetted areas of A_p^u and A_p^l and volumes of V_b^u and V_b^l
(d)
Upper and lower contact lines L^u and L^l

Fig. 5

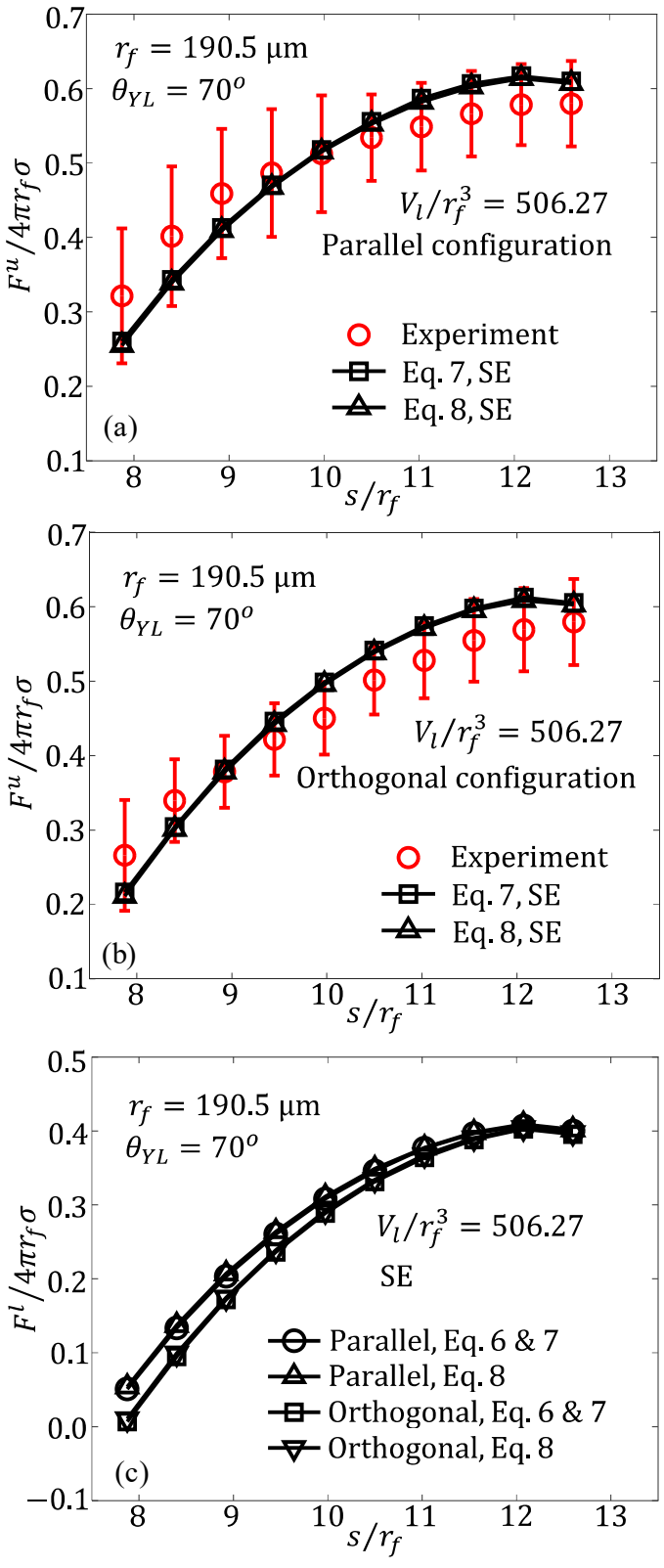
r_f = 190.5 μm
$\theta_{YL} = 70^o$
$V_l/r_f^3 = 506.27$
Parallel configuration
Experiment
Eq. 7, SE
Eq. 8, SE
(a)
$F^u/4\pi r_f\sigma$
s/r_f
r_f = 190.5 μm
$\theta_{YL} = 70^o$
$V_l/r_f^3 = 506.27$
Orthogonal configuration
Experiment
Eq. 7, SE
Eq. 8, SE
(b)
$F^u/4\pi r_f\sigma$
s/r_f
r_f = 190.5 μm
$\theta_{YL} = 70^o$
$V_l/r_f^3 = 506.27$
SE
Parallel, Eq. 6 & 7
Parallel, Eq. 8
Orthogonal, Eq. 6 & 7
Orthogonal, Eq. 8
(c)
$F^l/4\pi r_f\sigma$
s/r_f

Fig. 6

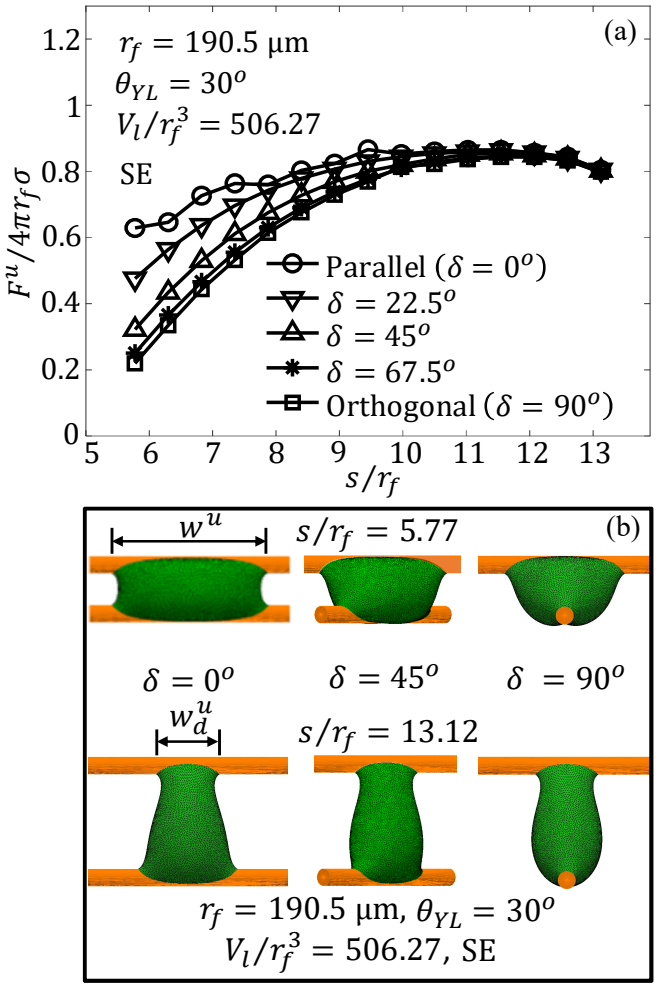
(a)
$r_f = 190.5$ μm
$\theta_{YL} = 30^o$
$V_l/r_f^3 = 506.27$
SE
Parallel ($\delta = 0^o$)
$\delta = 22.5^o$
$\delta = 45^o$
$\delta = 67.5^o$
Orthogonal ($\delta = 90^o$)
$F^u/4\pi r_f\sigma$
s/r_f
(b)
w^u
$s/r_f = 5.77$
$\delta = 0^o$
$\delta = 45^o$
$\delta = 90^o$
w_d^u
$s/r_f = 13.12$
$r_f = 190.5$ μm, $\theta_{YL} = 30^o$
$V_l/r_f^3 = 506.27$, SE

Fig. 7

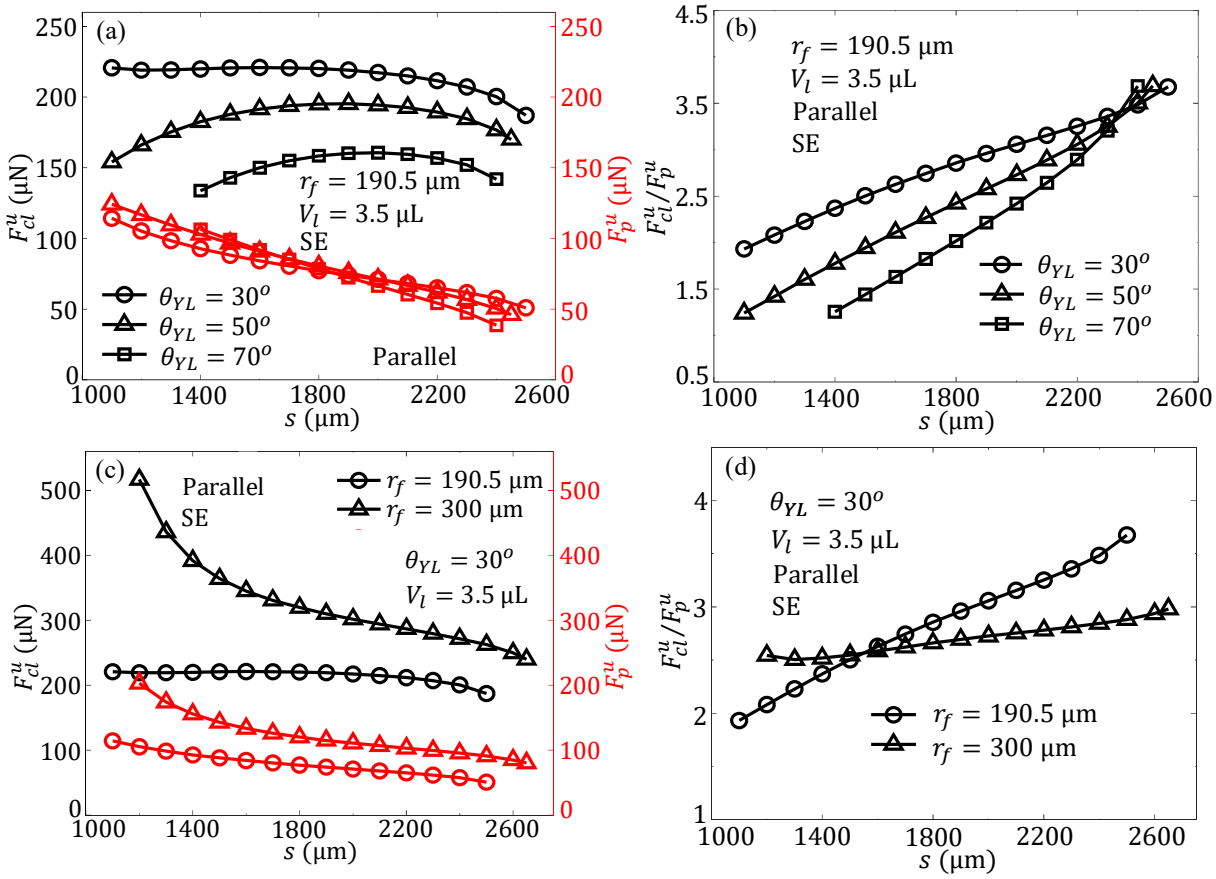
(a)
r_f = 190.5 μm
V_l = 3.5 μL
SE
Parallel
$\theta_{YL} = 30^o$
$\theta_{YL} = 50^o$
$\theta_{YL} = 70^o$
F_{cl}^u (μN)
F_p^u (μN)
s (μm)
(b)
r_f = 190.5 μm
V_l = 3.5 μL
Parallel
SE
F_{cl}^u/F_p^u
(c)
Parallel
SE
r_f = 190.5 μm
r_f = 300 μm
$\theta_{YL} = 30^o$
V_l = 3.5 μL
(d)
$\theta_{YL} = 30^o$
V_l = 3.5 μL
Parallel
SE
r_f = 190.5 μm
r_f = 300 μm

Fig. 8

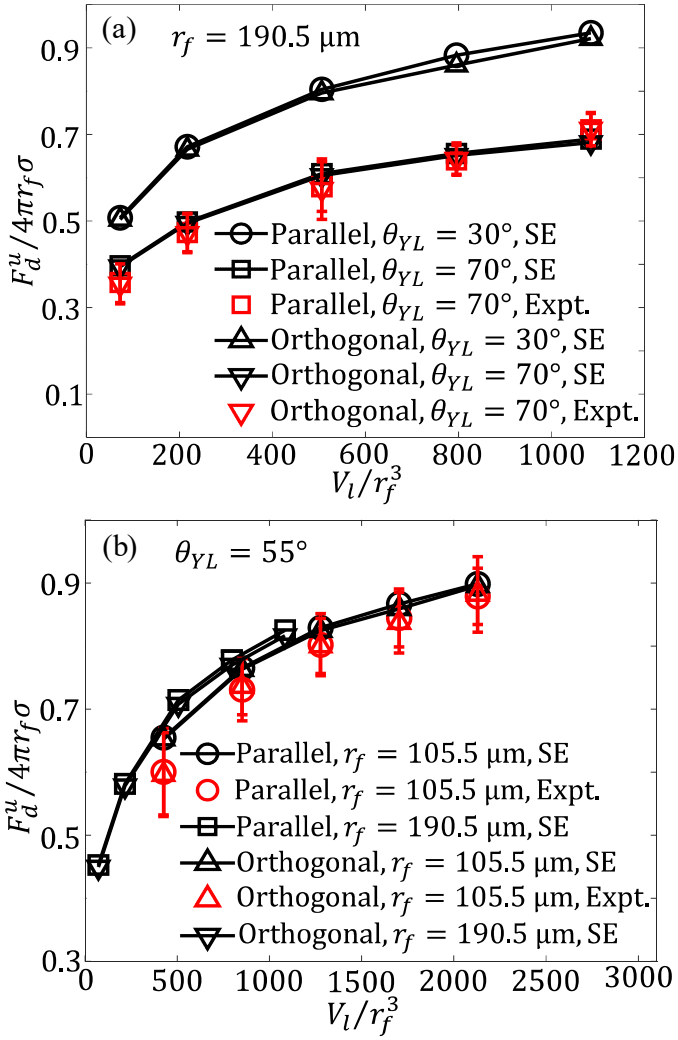
(a)
r_f = 190.5 μm
$F_d^u/4\pi r_f\sigma$
V_l/r_f^3
Parallel, θ_{YL} = 30°, SE
Parallel, θ_{YL} = 70°, SE
Parallel, θ_{YL} = 70°, Expt.
Orthogonal, θ_{YL} = 30°, SE
Orthogonal, θ_{YL} = 70°, SE
Orthogonal, θ_{YL} = 70°, Expt.
(b)
θ_{YL} = 55°
Parallel, r_f = 105.5 μm, SE
Parallel, r_f = 105.5 μm, Expt.
Parallel, r_f = 190.5 μm, SE
Orthogonal, r_f = 105.5 μm, SE
Orthogonal, r_f = 105.5 μm, Expt.
Orthogonal, r_f = 190.5 μm, SE

Fig. 9

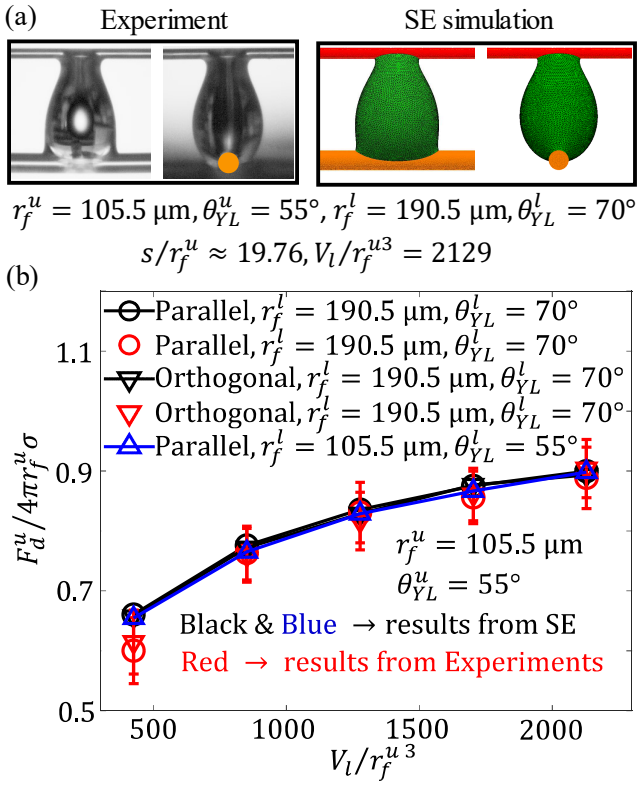
(a)
Experiment
SE simulation
$r_f^u = 105.5\ \mu m, \theta_{YL}^u = 55°, r_f^l = 190.5\ \mu m, \theta_{YL}^l = 70°$
$s/r_f^u \approx 19.76, V_l/r_f^{u3} = 2129$
(b)
Parallel, $r_f^l = 190.5\ \mu m, \theta_{YL}^l = 70°$
Parallel, $r_f^l = 190.5\ \mu m, \theta_{YL}^l = 70°$
Orthogonal, $r_f^l = 190.5\ \mu m, \theta_{YL}^l = 70°$
Orthogonal, $r_f^l = 190.5\ \mu m, \theta_{YL}^l = 70°$
Parallel, $r_f^l = 105.5\ \mu m, \theta_{YL}^l = 55°$
$r_f^u = 105.5\ \mu m$
$\theta_{YL}^u = 55°$
Black & Blue → results from SE
Red → results from Experiments
$F_d^u/4\pi r_f^u\sigma$
$V_l/r_f^{u\,3}$
1.1
0.9
0.7
0.5
500
1000
1500
2000

Fig. 10

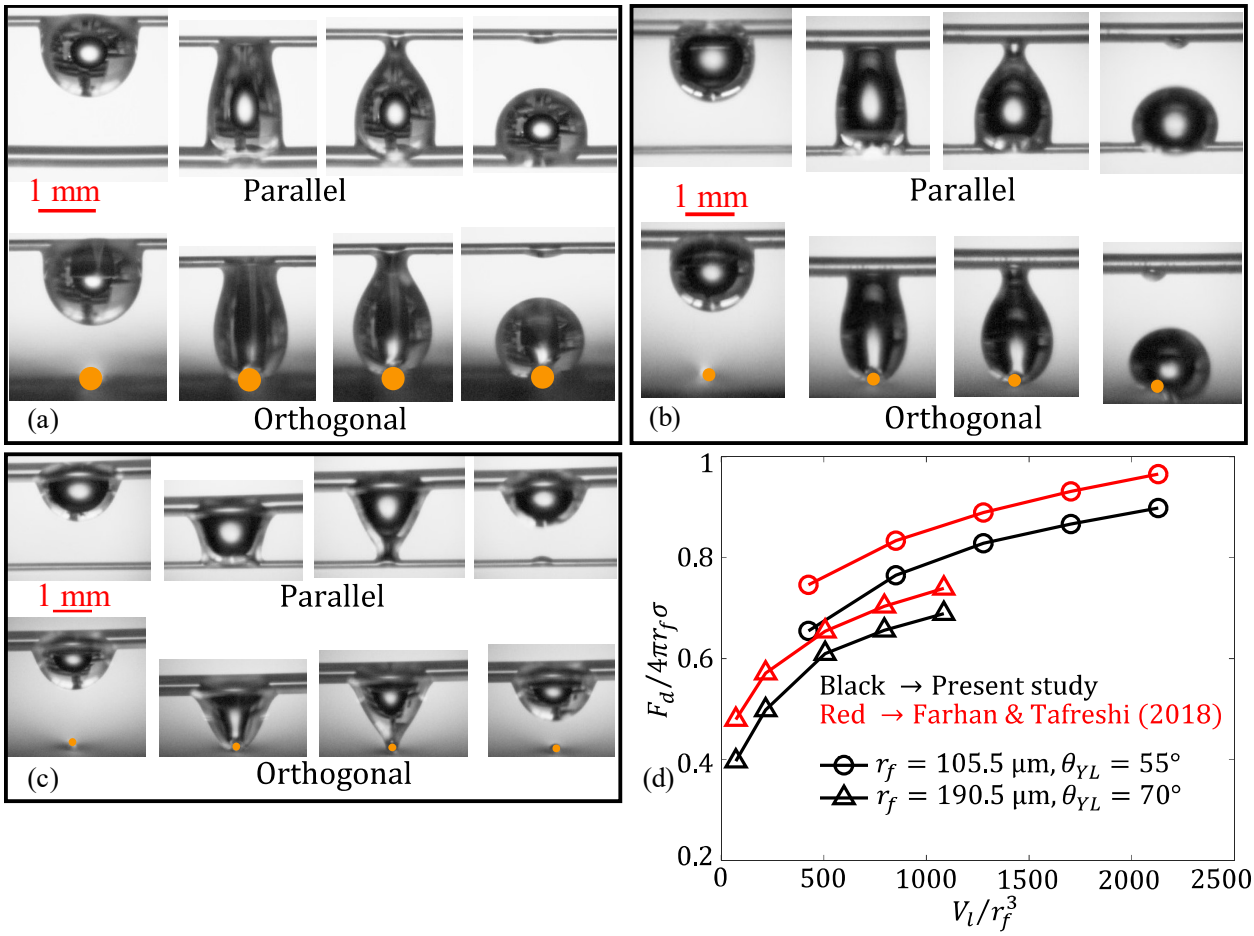
1 mm
Parallel
(a)
Orthogonal
1 mm
Parallel
(b)
Orthogonal
1 mm
Parallel
(c)
Orthogonal
(d)
$F_d/4\pi r_f\sigma$
V_l/r_f^3
Black → Present study
Red → Farhan & Tafreshi (2018)
r_f = 105.5 μm, θ_{YL} = 55°
r_f = 190.5 μm, θ_{YL} = 70°
0.2
0.4
0.6
0.8
1
0
500
1000
1500
2000
2500

Fig. 11

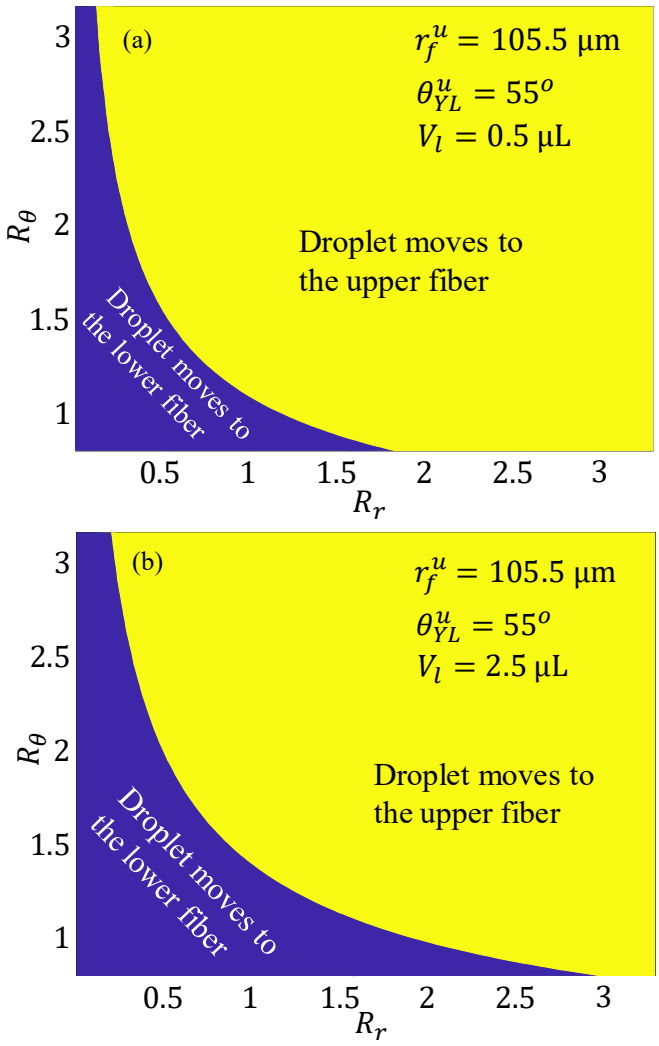
(a)
$r_f^u = 105.5$ μm
$\theta_{YL}^u = 55^o$
$V_l = 0.5$ μL
Droplet moves to the upper fiber
Droplet moves to the lower fiber
R_θ
R_r
3
2.5
2
1.5
1
0.5
1
1.5
2
2.5
3
(b)
$r_f^u = 105.5$ μm
$\theta_{YL}^u = 55^o$
$V_l = 2.5$ μL
Droplet moves to the upper fiber
Droplet moves to the lower fiber
R_θ
R_r

Fig. 12

TOC

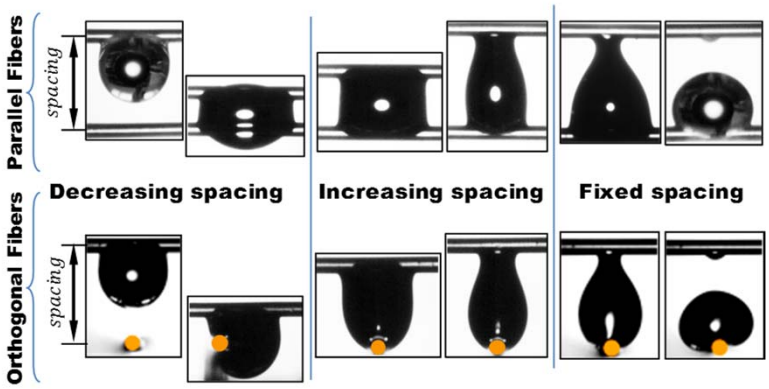
Parallel Fibers
spacing
Decreasing spacing
Increasing spacing
Fixed spacing
Orthogonal Fibers
spacing